



HAL
open science

A fast one-pot synthesise of crystalline anglesite by hydrothermal synthesis for environmental assessment on pure phase

Matthias Monneron–Gyurits, Emmanuel Joussein, Alexandra Courtin-Nomade, O. Grauby, Erwan Paineau, Solenn Reguer, Marilyne Soubrand

► To cite this version:

Matthias Monneron–Gyurits, Emmanuel Joussein, Alexandra Courtin-Nomade, O. Grauby, Erwan Paineau, et al.. A fast one-pot synthesise of crystalline anglesite by hydrothermal synthesis for environmental assessment on pure phase. *Environmental Science and Pollution Research*, 2021, 10.1007/s11356-021-17011-6 . hal-03629156

HAL Id: hal-03629156

<https://amu.hal.science/hal-03629156>

Submitted on 4 Apr 2022

HAL is a multi-disciplinary open access archive for the deposit and dissemination of scientific research documents, whether they are published or not. The documents may come from teaching and research institutions in France or abroad, or from public or private research centers.

L'archive ouverte pluridisciplinaire **HAL**, est destinée au dépôt et à la diffusion de documents scientifiques de niveau recherche, publiés ou non, émanant des établissements d'enseignement et de recherche français ou étrangers, des laboratoires publics ou privés.

35 under various physico-chemical conditions and sanitary risks. Finally, the paper allows to
36 obtain precise data on a pure phase in order to be able to more easily evaluate and understand
37 the role of anglesite in As-polluted sites and soils.

38

39 **Keyword:** hydrothermal synthesis, anglesite, characterization, spectroscopy, morphology,
40 environmental stability.

41

42 **Introduction**

43 Anglesite (PbSO_4) is a natural lead sulfate, described for the first time in 1783 by William
44 Withering (Zeman 1950). This mineral belongs to the barite group with a general formulation
45 $\text{A}(\text{SO}_4)$, where A may be Pb^{2+} , Ba^{2+} , Sr^{2+} or Cr^{2+} . The divalent atoms are 12-coordinated to
46 isolated SO_4 groups, which form regular tetrahedron. Their structures were first determined by
47 James and Wood (1925) indicating an orthorhombic form with the space group *Pnma*.

48 Anglesite is a typical oxidation by-product of galena (PbS) within lead ore deposits in supergene
49 environment (i.e. Boni et al., 2003; Mondillo et al., 2014) and is widely observed in Pb-mining
50 contexts as nanoparticles (e.g. Courtin-Nomade et al. 2016; Frau et al. 2009; Hayes et al. 2012).

51 In the environment, lead is known for its significant toxicity; the awareness of the behavior of
52 its different bearing phases thus appears to be a major health risk during ingestion or inhalation
53 (Pascaud et al. 2014). Since a lot of Pb-contaminated SUTMA (Soils of Urban, Industrial,
54 Traffic, Mining and Military Areas) are effective worldwide, it is of prime importance to
55 estimate the potential contribution of anglesite, a ubiquitous mining waste phase, in such
56 contaminated soils regarding potential sanitary risks as well as its behavior toward ingestion.

57 However, soil is well known to be a complex material due to the heterogeneity of its
58 composition in terms of chemical and mineralogical point of view, usually constituted of multi-
59 phases [e.g. quartz, feldspars, clay minerals and various metal(loïd)s bearing phases in a same
60 sample]. It is thus necessary to simplify this system in the way to better understand the
61 contribution of each mineral phases regarding their geochemical behavior or environmental
62 impact. In particular, what is the human sanitary risks contribution of anglesite from
63 contaminated soils? Therefore, the use of mineral synthesis is essential to obtain a pure product,
64 well characterized and as close as possible to the environmental phases. Indeed, the use of pure
65 phases is crucial in the environmental sciences, especially for a better understanding of the
66 sanitary impact related to the stability of anglesite in this case (Monneron--Gyurits et al. 2020).
67 Indeed, it is necessary to carry out specific tests on synthesized phases in order to estimate its
68 behavior over time, to know what controls its dissolution or stability (Pb release or not in human

69 bodies) and ultimately the crystallo-chemical effects when such (nano)particles are ingested or
70 inhaled into the human body.

71 In the literature, the protocols for synthesizing Pb phases are rarely or never explored,
72 particularly that of anglesite. The few protocols (Blount 1974; Wang et al. 2001; Xiang et al.
73 2005; Han et al. 2012) are based on Na_2SO_4 or CS_2 as the sulfur source. Moreover, these
74 protocols often imply laborious, and/or uneconomic experimental procedure either by using
75 high synthesis temperatures ~~([two-step process with calcination at $T = 600^\circ\text{C}$])~~ (Han et al. 2012;
76 Wang et al. 2001) or long time synthesis up to 7 days (Xiang et al. 2005)]. To overcome these
77 drawbacks, our study aims to propose a new protocol, easy to set up, to achieve pure crystalline
78 anglesite by soft hydrothermal synthesis in 1 day. The quick set-up of anglesite synthesis in
79 controlled conditions also represents a definite advantage in terms of various study for example
80 to get a sequence of different crystallite sizes, from micro- to nanoscale and to obtain new
81 thermodynamic and crystallographic data. Moreover, this type of sample may be used as
82 standard for various implementation and experiments typically for beamline database. To allow
83 a large number to apprehend the sanitary risks and especially to better reposition the role of
84 anglesite in environmental problems since this mineral is ubiquitous in polluted sites and soils,
85 the environmental stability of anglesite according to BCR and bioaccessibility (UBM protocols)
86 experiments has also been realized.

87

88 **Material and Methods**

89 *Synthesis experiment of anglesite*

90 Lead nitrate ($\text{Pb}(\text{NO}_3)_2$), iron sulfate ($\text{Fe}_2(\text{SO}_4)_3$) and 5% ammonium acetate were purchased
91 from Sigma Aldrich with an analysis grade quality (purity > 99%). A new synthesis way of
92 anglesite has been explored using the following protocol: 15g of $\text{Pb}(\text{NO}_3)_2$ used as Pb^{2+} source
93 and 6.95g of $\text{Fe}_2(\text{SO}_4)_3$ for the sulfate (SO_4^{2-}) source were weighted in two different polystyrene
94 dishes and directly mixed in same flat-bottom Teflon bomb reactor.

95 The mixing process were realized under magnetic stirring at 50 rpm. Then, 50 mL of ultrapure
96 water (UPW) produced by a Gradient A10 Milli-Q system (18.2m Ω) from Millipore (Bellerica,
97 MA, USA) was added to the previous mixture and mixed under magnetic stirring rotating at
98 110rpm for 10min to obtain a good homogenization. The pH value of the solution should be
99 stabilized at 1 (± 0.1 pH unit) before sealing the Teflon bomb reactor by adjusting it from
100 dropwise addition of HNO_3 1M or NaOH 1M under continuous stirring. Finally, the autoclave
101 is placed in a Memmert UN30 oven pre-heated at 94°C . After 24h, the Teflon bomb reactor
102 was slowly cooled at ambient temperature (20°C) for 30min to bring the pressure inside the

103 reactor to ambient value before opening. The same experiment was also performed during 48h
104 of ageing. Then, the solid was separated from the solution by using cellulose paper filter
105 (Fisherbrand, grade quality 122) and washed sequentially 5 times with UPW (100mL) and 5%
106 ammonium acetate to eliminate the excess of ferric sulfate ($[\text{Fe}_2(\text{SO}_4)_3]$). The last washing was
107 performed with 200mL of ultrapure water. Finally, the solid was placed in a glass vessel and
108 dried in an oven pre-heated at 40°C for 24h until the mass does not vary between two weightings
109 spaced by 2h.

110 *Analytical Methods*

111 X-ray diffraction (XRD), Fourier Transform Infrared spectroscopy (FTIR) and micro-Raman
112 investigations were performed at the CARMALIM analytical platform (CEC, Limoges,
113 France). The structural characterization was performed using XRD analysis. Experiments from
114 powder sample were carried out on a Bruker D8 advance diffractometer at the $\text{CuK}\alpha$
115 wavelength ($\lambda_{\text{K}\alpha}=0.1541$ nm), between 5 and 65° 2 θ with a 0.04° 2 θ step and a counting time
116 of 2 seconds/step. Prior to XRD experiments, the sample was gently grounded using a non-
117 amorphizer ball mill in zirconium oxide (Pulverisette 23, Fritsch). The obtained XRD patterns
118 were processed using EVA software (Bruker). Rietveld analysis was performed from the
119 method implemented in Profex BGMN software (Doebelin and Kleeberg 2015). Drawing of
120 the resulting structure was performed using VESTA software (Momma and Izumi 2011).

121 FTIR was performed on a Perkin Elmer FT-IR/NIR Frontier Spectrometer device operating in
122 Attenuated Total Reflectance (ATR mode), *i.e.* directly without further preparation, nor KBr
123 pellets. The ATR measurement was performed on powders in the mid infra-red region (600 -
124 4000 cm^{-1} range) at 2 cm^{-1} resolution for 15 scans.

125 A Jobin Yvon 6400 was used to perform the Raman spectroscopic analysis. The sample was
126 gently crushed and placed onto a glass chip. A 514nm Argon laser with an incidence power
127 limited at 5mW to avoid any destruction of the analyzed material was used as excitation source.
128 The analysis was performed using a $\times 50$ objective at room temperature from 100 to 1250 cm^{-1}
129 analytical region. Three different windows with an acquisition time ranging from 30s to 200s
130 and three iterations were used in the way to obtain a perfect sensibility and Raman resolution.
131 The microscopic investigations were done at CINaM/Aix-Marseille University, France. The
132 morphology of anglesite was performed by Scanning Electron Microscopy (SEM) observations
133 with a JEOL 6320 F operated at 15 kV and at low voltage 1kV. Samples were coated with
134 carbon prior analysis. JEOL JEM 2011 Transmission Electron Microscope (TEM) working at
135 200 kV was also used. The parameters were 50000 \times magnification, 20° tilt angle toward the
136 EDX detector, energy range of 40 keV, corrected counting time of 30 s, constant beam density

137 ~63.5 pA.cm⁻². Elements were quantified using the Bruker AXS TEM line mark data semi-
138 quantification procedure (Berthonneau et al. 2014). EDX chemical analyses were performed on
139 20 individual particles. The size of the particles was manually measured on micrographs using
140 ImageJ software.

141 The local structure of synthetic anglesite was investigated by X-ray Absorption Spectroscopy
142 experiments at the Pb LIII-edge (E₀=13035eV) on the DIFFABS beamline (synchrotron
143 SOLEIL, France). The X-ray beam was monochromated with a Si(111) double crystal with a
144 beam focalization assured by Kirkpatrick-Baez mirrors. The energy range was selected between
145 13000 and 13200eV with an energy step of 0.3eV. XANES spectrum was calibrated with a
146 metallic Pb foil at the Pb L-edge (13035keV). Anglesite sample was transferred in a borosilicate
147 capillary before analysis in fluorescence mode using a 4-elements silicon drift detector (Vortex-
148 ME4®). The XANES spectrum was obtained after standard procedures for pre-edge subtraction
149 and normalization using ATHENA software package (Ravel & Newville, 2005). EXAFS data
150 analysis was achieved by fitting the Fourier transformed experimental data with simulations
151 performed with the IFEFFIT code (Ravel & Newville 2005) based on the crystallographic
152 structure obtained from Rietveld refinement.

153 Sequential extractions were realized according to the Commission of the European
154 Communities Bureau of Reference (BCR) protocol (Auret et al. 1999) using a microwave
155 modified procedure (Pérez-Cid et al. 1998). The detailed protocol can be found in **Table S11**.
156 Briefly, 0.5 g of anglesite was successively mixed with 0.11 M of acetic acid (purity > 99%)
157 (F1 step corresponding to the acid-soluble/exchangeable fraction); 0.10 M of
158 hydroxylammonium (purity > 98%) at pH 2 (F2 step i.e. the reducible fraction relative to metal
159 bound to oxyhydroxides of iron and manganese); and 30% hydrogen peroxide (purity 32%) and
160 1 M ammonium acetate (purity > 98%) at pH 2 (F3 step i.e. the oxidizable fraction
161 corresponding to contaminants associated to organic matter or in sulfide form). After each step,
162 centrifugation (3300g for 15 min) was done, and the supernatant recover after 0.45 µm filtration
163 previous Pb analysis.

164 Bioaccessibility tests were performed to assess anglesite behavior in human gastro-intestinal
165 tract in the way to simulate the human physicochemical conditions (pH, temperature, contact
166 time, L/S ratio, and chemical composition) during anglesite accidental ingestion using the
167 unified BARGE protocol (UBM; Denys et al. 2009) since this protocol has been validated from
168 *in vivo* tests for Pb. Briefly, 0.6 g of anglesite were subjected to the gastric extraction (saliva +
169 gastric fluid; L/S = 37.5) and then to gastro-intestinal extraction (saliva, gastric fluid, bile,
170 duodenal fluid; L/S = 37.5) to highlight the difference between gastric and gastro-intestinal

171 bioaccessibility. The **Table SI 2** summarized the procedure details. The bioaccessibility results
172 is calculated along percentage of total element content.

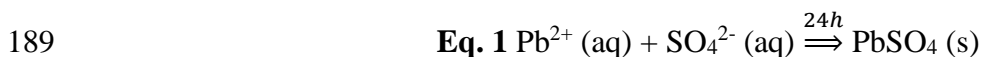
173 After BCR and UBM extractions, Pb contents in solution were analyzed by Atomic Absorption
174 Spectrometry using a spectrometer Variant 220FS (FAAS) with a quantification limit for Pb of
175 0.5 mg L. Pb standards of 1 g L were used for calibration (Certipur Merck), and the BCR-483
176 sewage sludge-amended soil (trace elements) are used in the way to validate the analyses. All
177 the analysis were conducted in duplicate.

178

179 **Results and discussion**

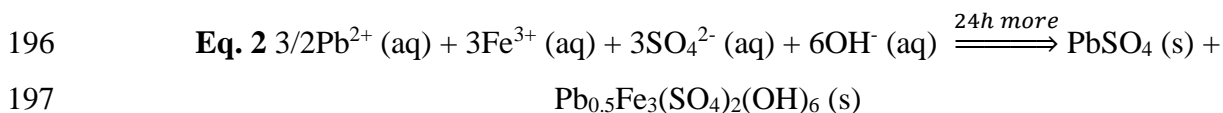
180 *Time synthesis, purity and processing*

181 The X-ray diffraction pattern of as-synthesized material is presented in **Fig. 1**. Indexation of all
182 peaks is consistent with orthorhombic crystalline anglesite (JCPDF 01-089-7356) with the main
183 peaks located at 20.81, 26.73 and 29.70°2θ. Analysis of the XRD pattern also indicates that our
184 synthetic sample has a high degree of purity without by-products, such as plumbojarosite, ferric
185 sulfate or amorphous phases. Assuming a complete conversion of precursors as ionic forms in
186 liquid phase (the Solubility Product Constants (K_{sp}) of involved lead sulfate salt at normal
187 conditions for PbSO₄ is K_{sp} = 1.6×10⁻⁸ from database WATEQ4F (Ball & Nordstrom 1991),
188 then the chemical reaction (**Eq. 1**) can be written simply as:



190 Beyond a fast synthesis process, another benefit of the proposed protocol is that the mass yield
191 of the reaction is close to 55% after washing. Note that after 48h of hydrothermal treatment
192 (**Fig. SI 1**), some additional reflection arising from impurities of plumbojarosite (JCPDF 00-
193 039-1353) are detected at 14.42, 29.09 and 34.41°2θ. The resulting chemical reaction is the
194 continuity of **Eq. 1** and can be written according to the following **Eq. 2**:

195



198 This reaction (**Eq. 2**) is due to (i) the simultaneous presence of PbSO₄ and Fe₂(SO₄)₃ during the
199 reacting process (Dutrizac et al. 1980) and to (ii) the change of the Eh (redox potential)
200 conditions during time synthesis. Indeed, according to the Eh–pH diagram for part of the system
201 S-O-Fe-Pb-H₂O (e.g. Forray et al. 2010; **Fig. SI 2**), the stability domain (Eh-pH) of anglesite
202 in acidic condition is limited. The variation of the pH and Eh values has been measured along
203 48h, the results evidence that (i) a small decrease of pH value from 0 to 48h inducing a loss of

204 0.2 unit pH (0.9 to 0.7), and (ii) a slight increase of the Eh value is noted (increase of 100 mV
205 from 24 (500 mV) to 48h (600mV), probably due to the effect of plumbojarosite
206 nucleation/growth. This is clearly enough to get out of the stability range of the anglesite and
207 therefore closer to that of the plumbojarosite. Consequently, up to 24 hours, the conditions of
208 nucleation/growth of the anglesite are optimal but induces a slight physico-chemical
209 modification of the system, favoring the subsequent precipitation of plumbojarosite to the
210 detriment of the anglesite. Note that this hydrothermal synthesis mode is interesting because it
211 is possible to obtain easily reproducible properties and structural characteristics of anglesite.
212 Moreover, it can be possible to control both the size and the crystallinity of the samples which
213 is a significant plus. Accordingly, sample synthesized after 24 h is the one that has been
214 characterized precisely characterize using multi techniques approach described above.

215

216 *Structural characterization of pure synthesized anglesite*

217 Rietveld experiment has been performed in the way to obtain structural cell parameters of the
218 synthetic samples. The structural characterization is well reproduced with the orthorhombic
219 *Pbnm* $Z = 4$ structure of anglesite. The lattice parameters of the obtained PbSO_4 unit cell are
220 reported in the **Table 1** ($a = 6.95225 \text{ \AA}$, $b = 8.47558 \text{ \AA}$, $c = 5.39800 \text{ \AA}$) and are in accordance
221 with conventional parameters of anglesite found in the literature on both synthetic (Antao 2012)
222 or natural phases (Jacobsen et al. 1998). Finally, the structure parameters determined from
223 Rietveld refinement are presented in **Table 2** and the corresponding 3D structure is reported in
224 **Fig. 2**.

225 Spectroscopic investigations by coupling FTIR, Raman and XANES measurements are
226 reported in **Fig. 3a** and **3b**, respectively. Firstly, it seems that there is no real difference between
227 reference data from literature and the synthesized one relative to the morphology of the spectra.
228 The characteristic bands of anglesite are only presented between 600 cm^{-1} and 1400 cm^{-1} in the
229 FTIR spectrum (**Fig. 3a**). The sharp band at 625 cm^{-1} is related to the stretching vibration bands
230 ν_4 (SO_4^{2-}) while the bands located at 965 cm^{-1} , 993 cm^{-1} and 1166 cm^{-1} are respectively
231 attributed to ν_1 , ν_3 and ν_3 modes of (SO_4^{2-}) (Farmer 1977; Lane 2007). The Raman spectrum
232 (**Fig. 3b**) highlights seven main bands located at 1155, 1060, 973, 640, 605, 449, 438, which
233 can be assigned to ν_3 , ν_3 , ν_1 , ν_4 , ν_4 , ν_2 , ν_2 (SO_4^{2-}) respectively and 132 cm^{-1} to lead sulfate
234 (position refers are in accordance with RRuff database).

235 To go further, the XAS spectrum of this sample was carried out at the Pb-L_{III}-edge (**Fig. 4**).
236 Experimental XANES spectrum (**Fig. 4a**) displays a typical white-line at 13044eV followed by
237 a first oscillation centered around 13079eV in agreement with previous studies (*e.g.* Hayes et

238 al. 2012; Sanderson et al. 2015). The broad shape may be related to the degree of covalent
239 bonding in Pb anglesite as well as the symmetry of Pb(II) sites. The first derivative spectrum
240 displays a peak at 13037 eV, indicative of the $2p \rightarrow 6d$ transition in the Pb(II) form.

241 Even if the purpose of the article is not to make an EXAFS modelling of the anglesite,
242 experimental EXAFS oscillations are shown in **Fig. 4b** and **4c** and the parameters of fit are
243 reported in **Table 3**. RDF curves present a first peak centred at 2\AA , related to oxygens atoms
244 surrounding lead. For higher distances, a broad band is evidenced near 4\AA . EXAFS spectrum
245 was fitted using backscattering paths extracted from the refined atomic structure determined
246 from XRD. Although anglesite exhibits a low signal/noise ratio for high k values, the simulated
247 curve shows a satisfactory agreement with experimental data, especially for the first
248 coordination shell composed of 12 oxygen atoms.

249 Finally, the morphology of synthetic anglesite particles has been investigated by SEM and TEM
250 observations as illustrated in **Fig. 5a, 5b, 5c** and **Fig. 5d, 5e, 5f, 5g** respectively. The main type
251 of morphology presenting same chemical analysis (not shown; but in accordance with
252 theoretical structural formula) is sticks-like structure (**Fig. 5a-c**) of about 0.6 to $3\mu\text{m}$ long (mean
253 704 nm length from measurement of 25 isolated particles by TEM) with width of approximately
254 0.1 to $1\mu\text{m}$ (mean 174 nm width from measurement of 25 isolated particles by TEM). It seems
255 that the crystals are mostly thin to thick tabular probably from crystal structure along the $\{001\}$,
256 commonly with $\{210\}$, $\{101\}$ in accordance with the works of Ma et al. (2011) and Stoll (2010).
257 Interestingly, the synthesized anglesite obtained in this study present a polyhedral structure
258 morphology close to those obtained at pH 1.5 reported in the work of Ma et al. (2011). This
259 result strongly suggests the importance of the pH during the synthesis since it has been proposed
260 that increasing the pH of the reaction induces a modification of the crystal shape (Ma et al.
261 2011).

262 The TEM morphologies (**Fig. 5d** and **5e**) exhibit particles with poorly defined faces and a length
263 of about $1\mu\text{m}$ for a width of about 200 nm. It is worth noting the presence of some blocky
264 particles which correspond easily to what has been observed in SEM but of small size.

265 The SAED plates (**Fig. 5f**) correspond well to an orthorhombic structure in adequacy with the
266 structure of the anglesite. The structural formulae from EDX (**Fig. 5g**) are quite closed to pure
267 anglesite, *i.e.* Pb_1SO_4 and the analysis confirm the purity of sample without the presence of Fe
268 in the structure.

269

270 *Environmental stability and bioaccessibility of synthetic anglesite*

271 The BCR extraction is used to evaluate the potential environmental stability of anglesite under
272 various physico-chemical conditions traducing a short- and long-term behavior. Indeed, the
273 short term $F_{\text{acid soluble}}$ mobilizable fraction is nice to understand the behavior of anglesite during
274 rapid condition changes such as rainy episodes relative to the possible exchangeable cationic
275 process. Moreover, the sum of the three first fractions ($F_{\text{acid soluble}} + F_{\text{reductible}} + F_{\text{oxidable}}$) is
276 representative of the long-term mobilization, simulating various environmental conditions. The
277 results of the distribution of lead according to BCR sequential extraction protocol are 0.25% (\pm
278 0.3%) – 1462 mg/kg (\pm 53 mg/kg), 0.75% (\pm 0.25%) – 5440 mg/kg (\pm 56 mg/kg) and 3% (\pm
279 0.3%) – 20195 mg/kg (\pm 742 mg/kg) for $F_{\text{acid soluble}}$, $F_{\text{reductible}}$ and F_{oxidable} respectively,
280 highlighting that residual fraction is predominant, the long-term mobilization ($F_{\text{acid soluble}} +$
281 $F_{\text{reductible}} + F_{\text{oxidable}}$) no exceed 4% - 27097 mg/kg of the total Pb content, so the main part is
282 found in residual fraction, which is the most stable. Except that the residual fraction, the second
283 dominant fraction is the oxidizable (F_{oxidable}) with 3%. Finally, the BCR extractions results
284 highlight a good environmental stability for anglesite with a residual fraction near 96% in
285 accordance with the works of Pascaud et al (2015).

286 The UBM bioaccessibility results of human gastro-intestinal matrix of anglesite is close to 3%
287 (\pm 0.3%) - 20100 mg/kg (\pm 2000 mg/kg) of Pb content and 0.45% (\pm 0.05%) - 2500 mg/kg (\pm
288 150 mg/kg) for the gastro-intestinal bioaccessibility one. The behavior of anglesite highlights a
289 decrease of the gastro-intestinal bioaccessibility, traducing that more than 96% of Pb is stable
290 in the gastrointestinal tract. These differences in dissolution can be explained by the difference
291 in pH values and by the ionic strength provided by the salts. These results are in accordance
292 with Ruby et al. (1992) for gastric fluid and traduces the small bioaccessibility of Pb into gastro-
293 intestinal tract which limit the contaminant assimilation. Finally, the long-term mobilization
294 ($F_{\text{acid soluble}} + F_{\text{reductible}} + F_{\text{oxidable}}$ from BCR experiments) correspond to the bioaccessible part.
295 This fact can be explained by the increase of pH value during gastro-intestinal phases which
296 dissolves anglesite due to the increases of Pb leaching (higher solubility between pH 5 to 9).
297 As already supposed in other studies (Zárate-Gutiérrez and Lapidus 2014), the precipitation of
298 Pb oxy(hydroxy)des may be possible limiting the concentration of Pb in solution.

299

300 **Conclusion**

301 In summary, this paper aims to present a new synthesis procedure and a complete physico-
302 chemical analysis of crystalline anglesite. The obtained results indicate that the final product
303 has a good crystallinity refers to XRD sharp peak with a straight spectroscopic signature. But,
304 on the contrary to many other procedures using various reagents and solvents (Na_2SO_4 , CS_2 ,

305 sodium dodecyl sulfate, hexane), the proposed protocol only requires 2 reagents, lead nitrate
306 and ferric sulfate, short hydrothermal ageing at low temperature, and producing easily
307 interesting mass yield of synthetic anglesite. Structural characterization reveals that the
308 obtained synthetic anglesite can be used as a standard for spectroscopic analysis.

309 The environmental stability and bioaccessibility of anglesite have been done to evaluate
310 environmental stability of anglesite under various physico-chemical conditions and sanitary
311 risks. This makes it possible to have precise data on a pure phase in order to be able to more
312 easily evaluate and understand the role of anglesite, a ubiquitous mineral in As-polluted sites
313 and soils, when it is mixed with other phases, and thus to better understand the health risks.

314

315 **Acknowledgment**

316 We acknowledge all the DIFFABS staffs for assistance in using beamline DIFFABS at Soleil
317 Synchrotron, and Pr. M.E.S. Glaoui for his constructive remarks.

318

319 **Ethics approval and consent to participate**

320 Not applicable.

321

322 **Consent to Publish**

323 Not applicable.

324

325 **Authors Contributions**

326 Matthias MONNERON-GYURITS, Emmanuel JOUSSEIN, Alexandra COURTIN-
327 NOMADE, Olivier GRAUBY, Erwan PAINEAU, Solenn REGUER and Marilyne
328 SOUBRAND conceptualized the study, participated in the study design, collected the data and
329 revised the manuscript. All authors read and approved the final manuscript.

330

331 **Funding**

332 This study was funded by SOLEIL for provision of synchrotron radiation facilities (proposal
333 20171406), and The Soil Take Care SUDOE program (project UE-16-SOE1/P4/F0023).

334

335 **Competing interests**

336 The authors declare no competing interests.

337

338 **Availability of data and materials**

339 Anglesite may be available from the corresponding author on reasonable request.

340

341 **References**

342 Antao SM (2012) Structural trends for celestite (SrSO₄), anglesite (PbSO₄), and barite
343 (BaSO₄): Confirmation of expected variations within the SO₄ groups. *Am Min* 97:661–665.
344 <https://doi.org/10.2138/am.2012.3905>

345 Auret G, Lopez-Sanchez JF, Sahuquillo A, Rubio R., Davidson CM, Ure AM,
346 Quevauviller P (1999) Improvement of the BCR three step sequential extraction procedure prior
347 to certification of new sediment and soil reference materials. *J Environ Monit* 1:57-6.
348 <https://doi.org/10.1039/A807854H>

349 Ball JW, Nordstrom DK (1991) WATEQ4F – User’s manual with revised thermodynamic
350 data base and test cases for calculating speciation of major, trace and redox elements in natural
351 waters, U.S.G.S. Open-File Report 90-129, 1991.

352 Berthonneau J, Grauby O, Ferrage E, Vallet JM, Bromblet P, Dessandier D, Chaudanson
353 D, Baronnet A (2014) Impact of swelling clays on the spalling decay of building limestones:
354 Insights from X-ray diffraction profile modeling. *Eur J Mineral* 26:643-656.
355 <https://doi.org/10.1127/0935-1221/2014/0026-2393>

356 Blount CW (1974) Synthesis of Barite, Celestite, Anglesite, Witherite, and Strontianite
357 from Aqueous Solutions. *Am Min* 59:1209-1219.

358 Boni M, Gilg HA, Aversa G, Balassone G (2003) The “Calamine” of Southwest Sardinia:
359 Geology, Mineralogy, and Stable Isotope Geochemistry of Supergene Zn Mineralization. *Econ*
360 *Geol* 98:731–748. <https://doi.org/10.2113/gsecongeo.98.4.731>

361 Courtin-Nomade A, Waltzing T, Evrard C, Soubrand M, Lenain JF, Ducloux E, Ghorbel
362 S, Grosbois C, Bril H (2016) Arsenic and lead mobility: From tailing materials to the aqueous
363 compartment. *J Appl Geochem* 64:10–21. <https://doi.org/10.1016/j.apgeochem.2015.11.002>

364 Denys S, Caboche J, Feidt C, Hazebrouck B, Dor F, Dabin C, Floch-Barneaud A, Tack
365 K (2009) Biodisponibilité et bioaccessibilité des métaux et metalloïdes des sols pollués pour la
366 voie orale chez l’homme. *Environnement Risques et Santé* 8:433–438.
367 <https://10.1684/ers.2009.0291>

368 Doebelin N, Kleeberg R (2015) Profex: a graphical user interface for the Rietveld
369 refinement program BGMN. *J Appl Crystallogr* 48:1573–1580.
370 <https://doi.org/10.1107/S1600576715014685>

371 Dutrizac JE, Dinardo O, Kaiman S (1980) Factors affecting lead jarosite formation.
372 *Hydrometallurgy* 5:305–324. [https://doi.org/10.1016/0304-386X\(80\)90022-5](https://doi.org/10.1016/0304-386X(80)90022-5)

373 Farmer VC (1977) *Infrared Spectra of Minerals*. Mineralogical Society of Great Britain
374 & Ireland, London. <https://doi.org/10.1180/mono-4>

375 Forray FL, Smith AML, Drouet C, Navrotsky A, Wright K, Hudson-Edwards KA,
376 Dubbin WE (2010) Synthesis, characterization and thermochemistry of a Pb-jarosite. *Geochim*
377 *Cosmochim Acta* 74:215-224. <http://dx.doi.org/10.1016/j.gca.2009.09.033>

378 Frau F, Ardau C, Fanfani L (2009) Environmental geochemistry and mineralogy of lead
379 at the old mine area of Baccu Locci (South-East Sardinia, Italy). *J Geochem Explor* 100:105–
380 115. <https://doi.org/10.1016/j.gexplo.2008.01.005>

381 Han B, Xie A, Yu Q, Huang F, Shen Y, Zhu L (2012) Synthesis of PbSO₄ crystals by
382 hydrogel template on postprocessing strategy for secondary pollution. *Appl Surf Sci* 261:623–
383 627. <https://doi.org/10.1016/j.apsusc.2012.08.069>

384 Hayes SM, Webb SM, Bargar JR, O’Day PA, Maier RM, Chorover J (2012) Geochemical
385 Weathering Increases Lead Bioaccessibility in Semi-Arid Mine Tailings. *Environ Sci Technol*
386 46:5834–5841. <https://doi.org/10.1021/es300603s>

387 Jacobsen SD, Smyth JR, Swope RJ, Downs RT (1998) Rigid-body character of the SO₄
388 groups in celestine, anglesite and barite. *Canad Mineral* 36:1053–1060.

389 James RW, Wood WA (1925) The crystal structure of barytes, celestine and anglesite.
390 *Proc. R. Soc. Lond. A* 109:598–620. <https://doi.org/10.1098/rspa.1925.0148>

391 Lane MD (2007) Mid-infrared emission spectroscopy of sulfate and sulfate-bearing
392 minerals. *Am Min* 92:1–18. <https://doi.org/10.2138/am.2007.2170>

393 Lee JS, Wang HS, Lizuka Y, Yu SH (2005) Crystal structure and Raman spectral studies
394 of BaSO₄-PbSO₄ solid solution. *Z Kristall* 220:1-9. <https://doi.org/10.1524/zkri.220.1.1.58891>

395 Ma Y, Yang L, Shen Y, Xie A (2011) Morphology control of anglesite microcrystals with
396 polyhedron: Synthesis, growth mechanism, and optical properties. *Russ J Phys Chem* 85:1454–
397 1464. <https://doi.org/10.1134/S0036024411080334>

398 Momma K, Izumi F (2011) VESTA 3 for three-dimensional visualization of crystal,
399 volumetric and morphology data. *J Appl Crystallogr* 44:1272-1276.
400 <https://doi.org/10.1107/S0021889811038970>

401 Mondillo N, Boni M, Balassone G, Villa IM (2014) The Yanque Prospect (Peru): From
402 Polymetallic Zn-Pb Mineralization to a Non sulfide Deposit. *Econ Geol* 109: 1735–1762.
403 <https://doi.org/10.2113/econgeo.109.6.1735>

404 Monneron M, Soubrand M, Joussein E, Courtin-Nomade A, Jubany I, Casas S, Bahi N,
405 Faz A, Gabarron M, Acosta JA, Martinez-Martinez S (2020) Investigating the relationship
406 between speciation and oral/lung bioaccessibility of a highly contaminated tailing: contribution
407 in health risk assessment. *Environ Sci Pollut Res* 27:40732-40748. <https://doi.org/10.1007/s11356-020-10074-x>.

409 Pascaud G, Lévêque T, Soubrand M, Boussem S, Joussein E, Dumat C (2014)
410 Environmental and health risk assessment of Pb, Zn, As and Sb in soccer field soils and
411 sediments from mine tailings: solid speciation and bioaccessibility. *Environ Sci Pollut Res*
412 21:4254-4264. <https://doi.org/10.1007/s11356-013-2297-2>

413 Pérez-Cid B, Lavilla I, Bendicho C (1998) Speeding up of a three-stage sequential
414 extraction method for metal speciation using focused ultrasound. *Anal Chim Acta* 360:35–41.
415 [doi: 10.1016/S0003-2670\(97\)00718-6](https://doi.org/10.1016/S0003-2670(97)00718-6)

416 Ravel B, Newville M (2005) ATHENA, ARTEMIS, HEPHAESTUS: data analysis for
417 X-ray absorption spectroscopy using IFEFFIT. *J Synchrotron Radiat* 12:537-541.
418 <https://doi.org/10.1107/S0909049505012719>

419 Ruby M, Davis A, Kempton JH, Drexler J, Bergstrom PD (1992) Lead Bioavailability -
420 Dissolution Kinetics under Simulated Gastric Conditions. *Environ Sci Technol* 26:1242–1248.
421 [doi: 10.1021/es50002a614](https://doi.org/10.1021/es50002a614)

422 Sanderson P, Naidu R, Bolan N, Lim JE, Ok YS (2015) Chemical stabilisation of lead in
423 shooting range soils with phosphate and magnesium oxide: Synchrotron investigation.
424 *J Hazard Mater* 299:395–403. <https://doi.org/10.1016/j.jhazmat.2015.06.056>

425 Stoll H (2010) Ion Partitioning in Ambient-Temperature Aqueous Systems. The
426 Mineralogical Society of Great Britain and Ireland.

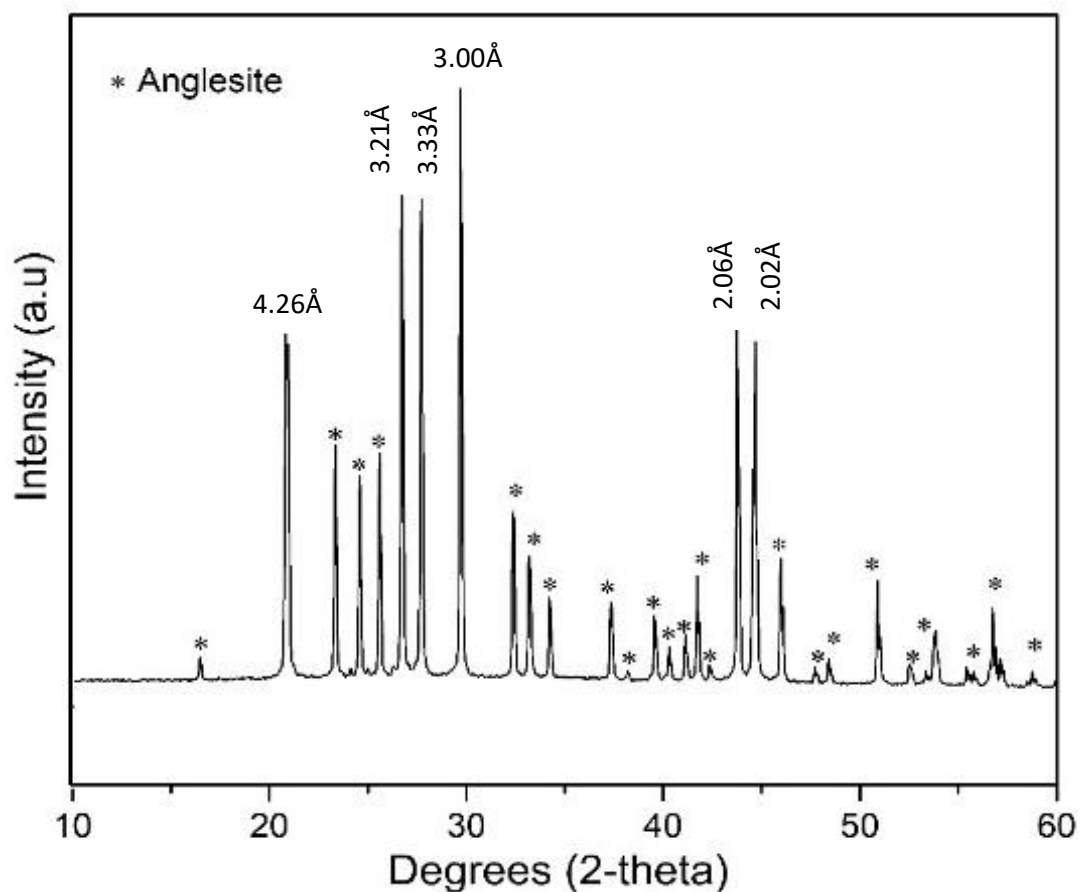
427 Wang HR, Lee JS, Yu SC (2001) Synthesis of zoning-free BaSO₄-PbSO₄ solid solution
428 and its structural characterizations. *Z Kristall* 217:143-148.

429 Xiang JH, Yu SH, Geng X, Liu BH, Xu Y (2005) Growth of PbSO₄ Single-Crystal
430 Nanorods and Optical Properties by a Microemulsion Approach. *Cryst Growth Des* 5:1157–
431 1161. <https://doi.org/10.1021/cg049630t>

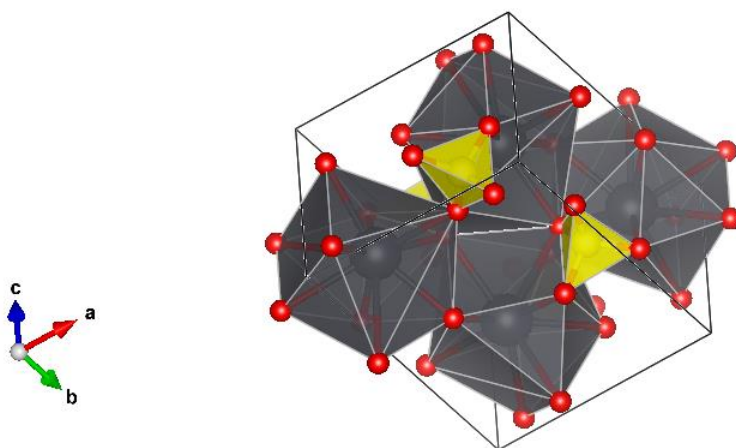
432 Zárte-Gutiérrez IR, Lapidus GT (2014) Anglesite (PbSO₄) leaching in citrate solutions.
433 *Hydrometallurgy* 144–145:124-128. doi.org/10.1016/j.hydromet.2014.02.003

434 Zeman F (1950) William Withering as a mineralogist: The Story of Witherite. *Bull Hist*
435 *Med* 24:530–538.

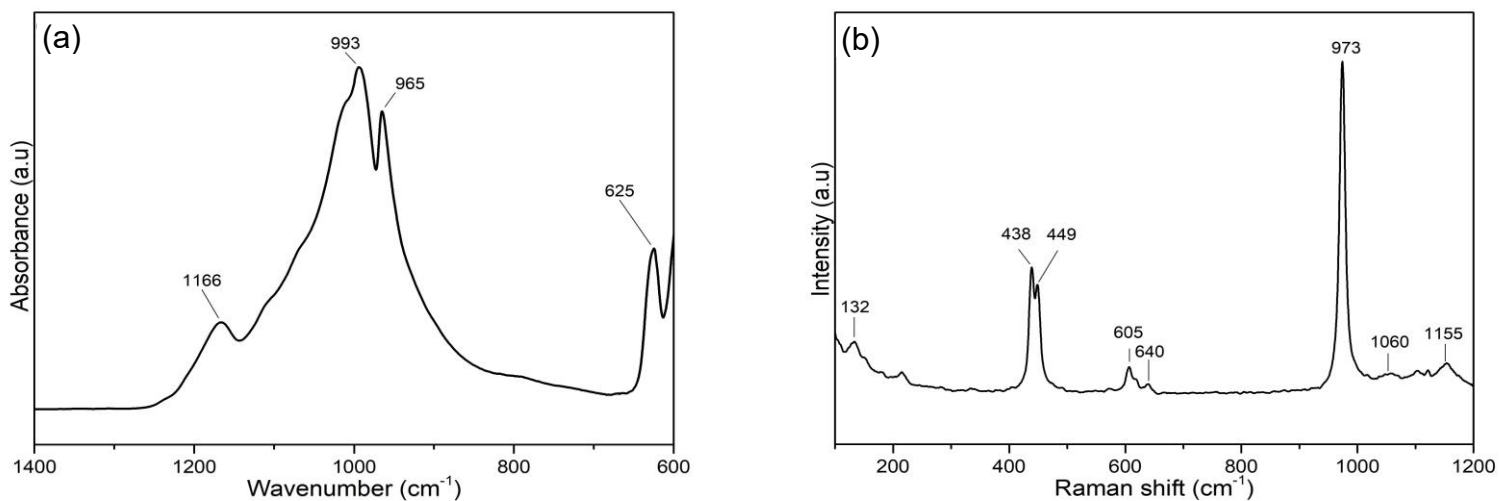
436



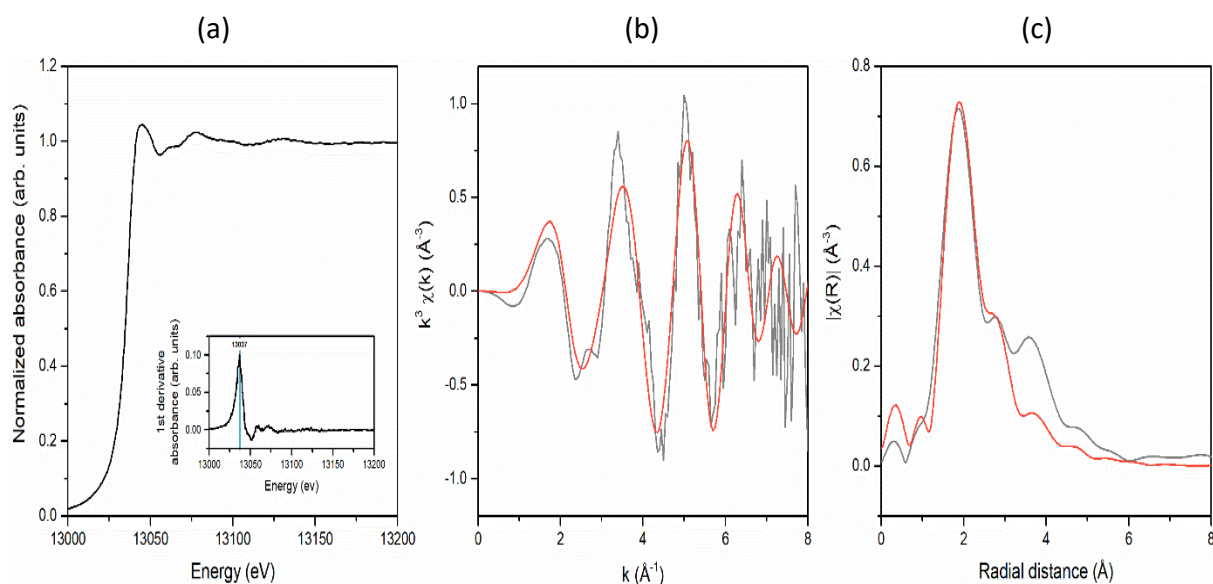
437 **Fig 1** XRD pattern of synthetic anglesite obtained after 24h of hydrothermal treatment. * refer
 438 to anglesite diffraction peaks, the position of main reflections are reported in Å.
 439



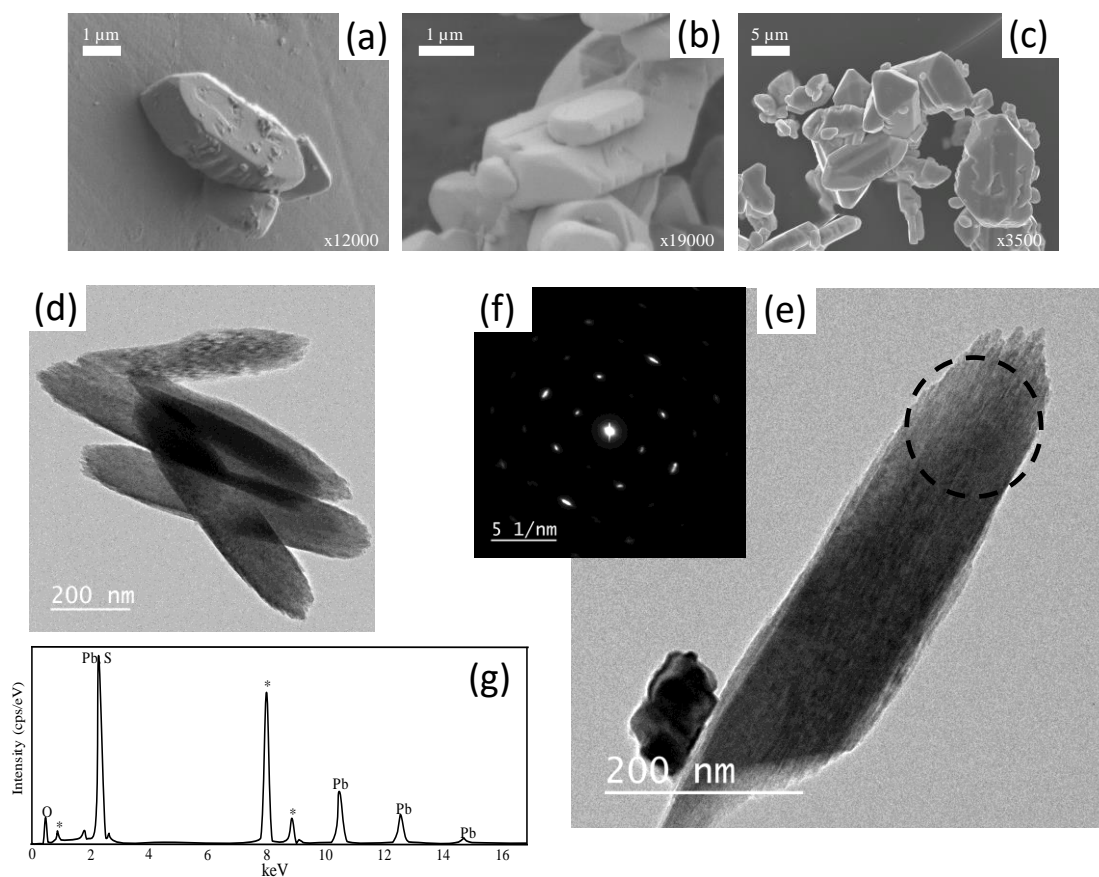
440
 441
 442 **Fig. 2** Structure of synthesized anglesite modeled from Rietveld refinement. Color code:
 443 lead (grey); sulfur (yellow); oxygen (red).



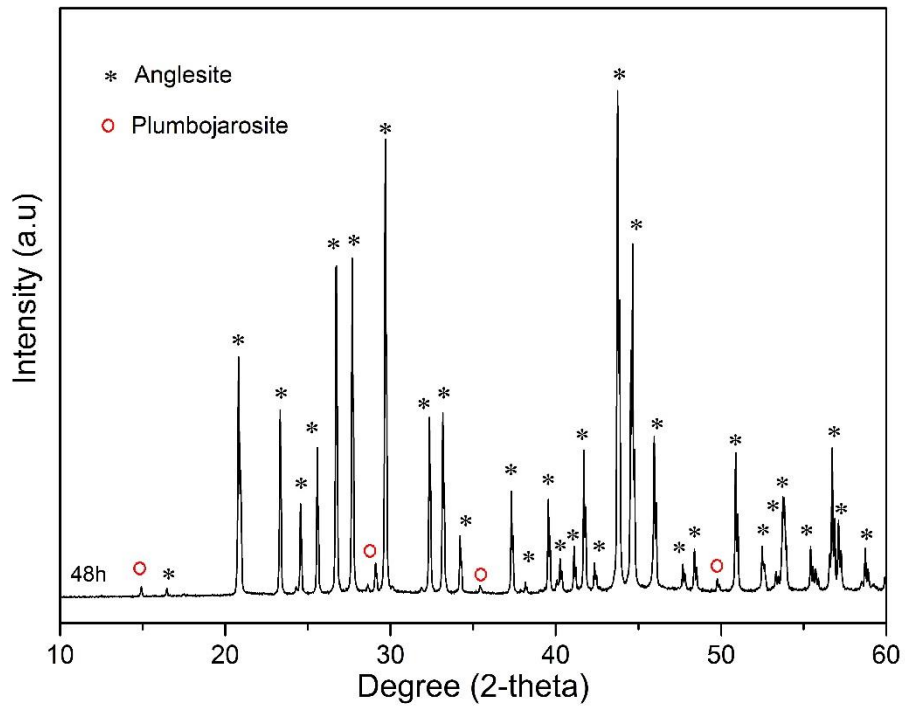
444
 445
 446 **Fig. 3** Characterization of the synthetic anglesite from (a) Infrared and (b) Raman
 447 spectroscopies.



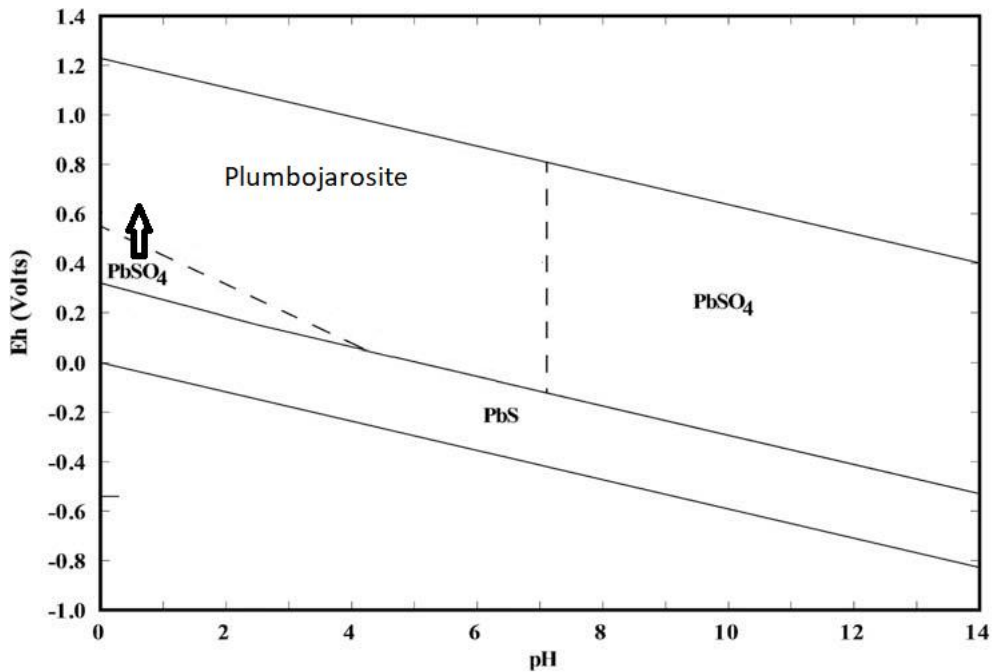
448
 449 **Fig. 4** (a) Normalized and first derivative XANES spectra at the Pb-L_{III} edge of the synthetic
 450 anglesite obtained after 24h of hydrothermal treatment, (b) Experimental Pb-L_{III} edge EXAFS
 451 oscillations, and (c) Radial Distribution Functions (black and red curves refer to experimental
 452 and the fitted one from Rietveld refinement data respectively).



453
 454 **Fig. 5** FEG-SEM images of the synthetic anglesite with different magnifications. (a) and (c)
 455 in lower secondary electron (LEI) and (b) in secondary electron in-lens (SEI). TEM images
 456 (d, e) of the synthetic anglesite at the same magnifications; (f) selected area electron
 457 diffraction (SAED) of the dotted line in (e), and (g) typical Energy Dispersive X-ray analysis
 458 on anglesite crystal. The star corresponds to copper grid.



459
 460 **Fig SI 1** XRD pattern of synthetic anglesite obtained after 48h of hydrothermal treatment. The
 461 presence of plumbojarosite is effective.



462
 463 **Fig. SI 2** Eh-pH diagram for part of the system S–O–Fe–Pb–H₂O at 25°C adapted from Forray
 464 et al. (2010). Note that in the case of this Eh-pH diagram, the assumed activities of dissolved
 465 species are 10⁻³ mol/L for S, Fe, and 10⁻⁸ mol/L for Pb. The arrow traduces the chemical change
 466 during time synthesis.

467 **Table 1** Lattice parameters a, b, c (Å) and unit-cell volume (Å³) determined from Rietveld
 468 refinement using BGMN software (angles a = b = c = 90°). Comparison with the literature: data
 469 obtained for Antao (2012) are from Aldrich product; Jacobsen et al. (1998) and James & Wood
 470 (1925) data after mineral collection, and from Lee et al. (2005) after synthesis.
 471

	a (Å)	b (Å)	c (Å)	V (Å ³)
This study	6.9522	8.4756	5.3980	318.074
Antao 2012	6.95802	8.48024	5.39754	318.486
Jacobsen et al. 1998	6.9549	8.4720	5.3973	318.03
James & Wood 1925	6.93	8.45	5.38	315.0
Lee et al. 2005	6.950	8.475	5.396	317.8

472

473

474 **Table 2** Structure parameters determined from Rietveld refinement using BGMN software.

475

	x	y	z	Occurrence	U
Pb	0.16722	0.18782	0.25000	1.000	0.019
S	0.18370	0.43620	0.75000	1.000	0.008
O1	0.09530	0.59210	0.75000	1.000	0.021
O2	0.04740	0.30720	0.75000	1.000	0.023
O3	0.30900	0.41910	0.97470	1.000	0.015

476 **Table 3** Parameters used to fit the EXAFS spectrum. N is the coordination number, R the radial
 477 distance and σ^2 the mean-square variation in path length.

478

Path index	Scattering atom(s)	N	R (radial distance)	σ^2 (Å ²)
1	Pb-O1.1	1	2.58905	0.02183
2	Pb-O2.1	3	2.62643	0.02183
3	Pb-O3.2	2	2.70207	0.02183
4	Pb-O3.3	2	2.89133	0.02183
5	Pb-O2.2	2	2.97481	0.02183
6	Pb-O1.2	2	3.23882	0.02183
7	Pb-S.1	2	3.39596	0.02749

479 **Table S11.** Protocol of the BCR sequential extraction.

480

Fraction	Chemical reagents	Volume (ml)	Solid-solution ratio (g/ml)	Sonication time and power
F1: acid-soluble/exchangeable fraction	Acetic acid (CH ₃ COOH) 0.11 mol/l	20	0.025	20 W for 7 min
F2: reducible fraction	Hydroxylammonium (HONH ₂ ·HCl) 0.10 mol/l (reagent brought back to pH 2 with nitric acid 69 %)	20	0.025	20 W for 7 min
F3: oxidizable fraction	Hydrogen peroxide (H ₂ O ₂) 30 %	10	0.05	20 W for 2 min
	Ammonium acetate (C ₂ H ₃ O ₂ NH ₄) 1 mol/l (reagent brought back to pH 2 with nitric acid 69 %)	25	0.02	20 W for 6 min

481
482
483
484
485

Table SI 2. Composition of the digestive solution used during the UBM bioaccessibility test.

Saliva	Gastric fluid	Bile	Duodenal fluid
KCl 89.6 g/l - 10 mL	NaCl 175.3 g - 15.7 mL	NaCl 175.3 g - 30 mL	NaCl 175.3 g - 40 mL
KSCN 20 g/l - 10 mL	NaH ₂ PO ₄ 88.8 g/l - 3 mL	NaHCO ₃ 84.7 g/l - 68.3 mL	NaHCO ₃ 84.7 g/l - 40 mL
NaH ₂ PO ₄ 88.8 g/l - 10 mL	KCl 89.6 g/l - 9.2 mL	KCl 89.6 g/l - 4.2 mL	KH ₂ PO ₄ 8 g/l - 10 mL
NaCl 175.3 g/l - 1.7 mL	CaCl ₂ ·2H ₂ O 22.2 g/l - 18 mL	HCl 37% g/g - 200 µL	KCl 89.6 g/l - 6.3 mL
NaOH 40 g/l - 1.8 mL	NH ₄ Cl 30.6 g/l - 10 mL	urea 25 g/l - 10 mL	MgCl ₂ 5 g/l - 10 mL
urea 25 g/l - 8 mL	HCl 37% g/g - 8.3 mL	CaCl ₂ ·2H ₂ O 22.2 g/l - 10 mL	HCl 37% g/g - 180 µL
α-Amylase - 145 mg	Glucose 65 g/l - 10 mL	Bovine albumine - 1 g	CaCl ₂ ·2H ₂ O 22.2 g/l - 9 mL
Uric acid - 15 mg	Glucuronic acid 2 g/l - 10 mL	Porcine bile	Bovine albumine - 1 g
Mucin - 50 mg	Urea 25 g/l - 3.4 mL		Pancreatin - 3 g
	Glucosamine hydrochlorite 33 g/l - 10 mL		Lipase - 0.5 g
	Bovine albumine - 1 g		
	Pepsin - 1 g		

← Gastric phase →
← Gastro-intestinal phase →

486
487
488